

The CMB angular power spectrum via component separation: a study on Planck data

C. Umiltà^{1,2,3}, J.F. Cardoso¹, K. Benabed¹, and M. Le Jeune⁴

¹ Institut d'Astrophysique de Paris, Sorbonne Université, CNRS (UMR7095), 98 bis Boulevard Arago, F-75014, Paris, France

² Sorbonne Universités, Institut Lagrange de Paris (ILP), 98 bis Boulevard Arago, 75014 Paris, France

³ University of Cincinnati, Cincinnati, Ohio 45221

⁴ APC, Univ Paris Diderot, CNRS/IN2P3, CEA/Irfu, Obs de Paris, Sorbonne Paris Cité, France

July 4, 2018

ABSTRACT

Aims. We investigate the extent to which foreground cleaned CMB maps can be used to estimate the cosmological parameters at small scales.

Methods. We use the SMICA method, a blind separation technique which works directly at the spectral level. In this work we focus on the small scales of the CMB angular power spectrum, which are chiefly affected by noise and extragalactic foregrounds, such as point sources. We adapt SMICA to use only cross-spectra between data maps, thus avoiding the noise bias. In this study, performed both on simulations and on Planck 2015 data, we fit for extragalactic point sources by modeling them as shot noise of two independent populations.

Results. In simulations we correctly recover the point source emission law, and obtain a CMB angular power spectrum that has an average foreground residual of one fifth of the CMB power at $\ell \geq 2200$. On Planck data, the recovered point source emission law corresponds to external estimates, with some offsets at the highest and lowest frequencies, possibly due to frequency decoherence of point sources. The CMB angular power spectrum residuals are consistent with what we find in simulations. The cosmological parameters obtained from the simulations and the data show offsets up to 1σ on average from their expected values. Biases on cosmological parameters in simulations represent the expected level of bias in Planck data.

Conclusions. The results on cosmological parameters depend on the detail of the foreground residual contamination in the spectrum, and need a tailored modeling of the likelihood foreground model.

Key words. component separation – Planck – noise – point sources

1. Introduction

The cosmic microwave background (CMB) is an important probe for cosmology, and in recent years a lot of effort has been dedicated to its extraction from available data. In particular, the CMB angular power spectrum can be used to constrain the cosmological parameters. The Planck mission provided the astronomical community with full-sky observations in nine frequency bands between 30 and 857 GHz. These data are extremely important for CMB science since they allow to characterize and separate the primordial CMB signal from the other astrophysical galactic and extragalactic emissions or *foregrounds*.

Separating the CMB from the foregrounds is a highly non trivial task, and a number of component separation methods has been conceived in the past years. The Commander method (Eriksen et al. 2004; Eriksen et al. 2008) performs a Bayesian exploration of a physical parametric model. The SEVEM method (Fernández-Cobos et al. 2012) fits a number of templates obtained from the data themselves, while the CCA (Bedini et al. 2005; Bonaldi et al. 2006) technique exploits the foregrounds spatial correlations to recover their emission law.

Blind techniques, that use no prior information on foreground emission, have been largely employed. The advantage of such an approach is that it does not need any assumption on the foreground contamination. We note that this is also the case for SEVEM. Among blind methods, NILC (Delabrouille et al.

2009; Basak & Delabrouille 2012, 2013), GNILC (Remazeilles et al. 2011) and more recently SILC (Rogers et al. 2016) and HILC (Sudevan et al. 2017) all exploit the ILC technique. The L-GMCA (Bobin et al. 2008, 2013) method exploits the sparsity of the data in the wavelet domain.

Another popular technique for blind source separation is the Independent Component Analysis (ICA), implemented by FastICA (Maino et al. 2002), which is based on the non-Gaussianity of the sources, BICA (Vansyngel et al. 2016) which implements ICA in a Bayesian framework and SMICA (Cardoso et al. 2008), which blindly recovers the sources spectra in the maximum likelihood sense. The effort in finding new tools for component separation is still on-going: for example the ABS blind method has been recently proposed (Zhang et al. 2016).

The *Planck Collaboration* has selected four different methods to perform component separation and produce CMB maps. These are Commander, NILC, SEVEM and SMICA (Planck Collaboration IX et al. 2016). Nevertheless, the cosmological analysis of the CMB is very sensitive to residual foreground contamination in the data. The angular power spectra derived from the four Planck CMB maps have a residual foreground content which prevents their use for cosmological purposes. In particular, the small scale residuals of unresolved point sources in these maps is not well characterized (Planck Collaboration XI et al. 2016). Among the four CMB maps released by the *Planck Collaboration*, the SMICA map has the lowest extragalactic contribution

at high- ℓ (Planck Collaboration IX et al. 2016). More importantly for this work, SMICA proceeds in two steps: a component separation at the spectral (harmonic) level is first performed, the result of which is then used to control the synthesis of the CMB map from its harmonic coefficients. It is the first step of SMICA—component separation at the spectral level—which is of interest in this contribution.

In this work, we shall consider variations on the SMICA method of component separation, targeting direct cosmological analysis, based on the following three ideas. First, we take advantage of the ‘data splits’ available in Planck products. By cross-correlating the two halves of a data split, one obtains spectral estimates which are free of noise bias (Hinshaw et al. 2003), at the cost of a reasonable variance increase.

Second, we build on the fact that the SMICA method is based on a statistical fit *in the spectral domain* of a model of independent spectra (CMB, foregrounds and noise), the cleaned-up CMB map being produced in a second (optional) step. In this work, we shall focus on the first step of spectral fitting, *i.e.*, the SMICA method is only used as a tool for the joint fit of all the auto- and cross-spectra of a set of frequency channels. In this way the CMB angular power spectrum is estimated directly from the data.

Third, we introduce constraints on some of the spectral components fitted by SMICA. In the standard operation of SMICA, the foreground contribution is fully unconstrained (Planck Collaboration XV et al. 2014). This design choice naturally targets the large scale galactic contamination, failing to remove accurately the extragalactic contamination, since the latter is subdominant with respect to the galactic one on a wide range of scales. In this work, we use a foreground model that targets the extragalactic emission of unresolved point sources. In particular, we model them as two independent populations with a shot noise angular power spectrum. This allows us to recover their emission law, at the price of a partial loss of blindness of the method.

The natural comparison of this work results is with the cosmological analysis of the *Planck Collaboration* (Planck Collaboration XI et al. 2016; Planck Collaboration XIII et al. 2016). Their high- ℓ likelihood (PlikTT) is based on the spectra of a few frequency channels with low foreground content, in the cleaner area of the sky and on a tailored scale range. In this likelihood, the residual foreground contamination is described by a set of templates controlled by a few parameters for each non-negligible astrophysical contribution. The extragalactic point sources are modeled with a free amplitude parameter at each frequency.

This paper is organised as follows. In Sect. 2, we introduce the foreground emissions relevant to this analysis. In Sect. 3, we present the SMICA method and how we adapt it to spectral component separation based on cross-spectra. In Sect. 4 we present the data used and in Sect. 5 we present the results of the SMICA fit. Finally we show cosmological parameters obtained from the fitted CMB angular power spectra in Sect. 6. Our conclusions are given in Sect. 7.

2. The astrophysical foregrounds

The Planck and WMAP satellites delivered a set of full sky maps in the $23 \leq \nu \leq 857$ GHz range. Component separation methods aimed at map reconstruction exploit a wide range of frequencies in order to ameliorate their cleaning efficiency close to the galactic center. In this work we want to obtain a CMB power spectrum with low foreground contamination in particular at small scales and with respect to extragalactic contamination. Even though we are interested in retaining the largest possible sky fraction,

the complexity of foreground contamination close to the galactic center is a considerable drawback and we prefer to exclude this region from the analysis. We limit ourselves to frequencies larger than 100 GHz, where lower frequency galactic contamination from free-free and synchrotron is negligible (Planck Collaboration et al. 2016a). We present here a brief description of the foreground contamination at the frequencies of interest of this work. The relevant foreground emissions at frequencies $\nu \geq 100$ GHz are the thermal dust emission from our galaxy, and the emission of background unresolved galaxies.

2.1. Thermal dust

The galactic dust is the dominant foreground at large scales for frequencies above 70 GHz (Ichiki 2014). Its emission law can be empirically described by a modified black-body:

$$I_\nu \propto \nu^{\beta_d} B_\nu(T), \quad (1)$$

where $B_\nu(T)$ is the Planck black-body spectrum at a temperature T , while β_d is the dust spectral index. The values of T and β_d vary across the sky: as a reference, we can consider a temperature $T = (19.4 \pm 1.3)$ K and an average spectral index $\beta_d = 1.6 \pm 0.1$ (Planck Collaboration XLVIII et al. 2016, Sect. 4.2.2).

We can describe the angular power spectrum of dust approximately as (Planck Collaboration XI et al. 2016, Sect. 3.3):

$$C_\ell^{dust} \propto \ell^{-2.6}, \quad (2)$$

thus the dust contribution drops quickly at small scales.

2.2. Extragalactic foregrounds

The extragalactic contamination, which is only relevant at small angular scales, comes essentially from background galaxies and clusters. The former produce the radio point sources and Cosmic Infrared Background (CIB) contamination, while the latter are responsible for the SZ effect. The SZ effect, which is the distortion on CMB photons produced by the interaction with the intra-cluster hot gas, is not well constrained by Planck data alone (Planck Collaboration XI et al. 2016). In the Planck likelihood analysis, this emission has been constrained by using SPT and ACT small scale data (Planck Collaboration XV et al. 2014) or by imposing a narrow prior (Planck Collaboration XI et al. 2016). The background galaxies instead are an important source of contamination in Planck data. The resolved sources are masked, but a background diffuse emission of unresolved point sources is still present in the maps.

These sources can be categorized in two types: red elliptical galaxies that emit essentially in the radio band and dusty star-forming galaxies, which are more luminous in the infrared (IR) and produce the CIB emission. The point source emission can be described by at least two contributions, a shot noise part, due to the average random distribution of galaxies, and a clustered part due to the fact that galaxies follow the matter distribution and are thus not evenly distributed on the sky. Contrary to the radio sources, which are well described by the shot noise model alone (Hall et al. 2010; Lacasa et al. 2012), the infrared clustered contribution is quite important, and we refer to it as clustered CIB. The shot noise contribution has a flat spectrum (Tegmark & Efstathiou 1996):

$$C_\ell^{shot} = C^{shot}. \quad (3)$$

The clustered CIB contribution can be represented by:

$$C_\ell^{\text{clustered}} = \ell^\alpha, \quad (4)$$

where $\alpha = -1.4$ for $\ell > 2500$, and is shallower at larger scales (Planck Collaboration XI et al. 2016, Sect. 3.3).

3. Spectral component separation

The SMICA method (Cardoso et al. 2008) (*Spectral Matching Independent Component Analysis*) is a blind component separation method that works at the spectral level. SMICA is one of the four component separation tools used by the *Planck Collaboration* for map reconstruction. SMICA works by adjusting a model $R_\ell(\theta)$ to a set of ‘spectral covariance matrices’ \hat{R}_ℓ derived from the data. These matrices are defined as follows.

Given a set of n observed sky maps in n frequency channels, we denote $y_{\ell m}^i$ ¹ their spherical harmonic coefficients ($i = 1, \dots, n$) and we denote $\mathbf{y}_{\ell m}$ the $n \times 1$ vector which collects them. These observations are made of signal $\mathbf{o}_{\ell m}$ and noise $\mathbf{n}_{\ell m}$:

$$\mathbf{y}_{\ell m} = \mathbf{o}_{\ell m} + \mathbf{n}_{\ell m}. \quad (5)$$

Using these $\mathbf{y}_{\ell m}$ coefficients, the auto- and cross spectra of the input maps can be computed and collected in $n \times n$ empirical spectral covariance matrices \hat{R}_ℓ defined as:

$$\hat{R}_\ell = \frac{1}{2\ell + 1} \sum_m \mathbf{y}_{\ell m} \mathbf{y}_{\ell m}^T. \quad (6)$$

These matrices contain at each angular frequency ℓ the auto-spectra of each channel in their diagonal entries and the respective cross-spectra in their off-diagonal entries.

The model $R_\ell(\theta)$ describes the expected value of the spectra in \hat{R}_ℓ , and it has a tunable level of blindness, depending on the problem at hand. We will later see its specifications for the present work. The parameters of the model are adjusted to the data through the spectral matching criterion described in the next paragraph.

3.1. Spectral matching criterion

The spectral fitting criterion used by SMICA is the likelihood obtained by assuming that all input sky maps jointly follow a Gaussian stationary distribution. By standard arguments, one finds that for full sky statistics, the joint likelihood depends only on $R_\ell(\theta)$ and is proportional to $\exp(-\phi(\theta))$ where:

$$\phi(\theta) = \frac{1}{2} \sum_\ell (2\ell + 1) \left[\text{trace}(\hat{R}_\ell R_\ell(\theta)^{-1}) + \log \det R_\ell(\theta) \right] + \text{cst}. \quad (7)$$

It is useful to notice that, up to a constant term, this is equal to :

$$\phi(\theta) = \sum_\ell (2\ell + 1) K(\hat{R}_\ell, R_\ell(\theta)) + \text{cst}', \quad (8)$$

where $K(R_1, R_2)$ is the Kullback-Leibler divergence defined as:

$$K(R_1, R_2) = \frac{1}{2} \left[\text{trace}(R_1 R_2^{-1}) - \log \det(R_1 R_2^{-1}) - n \right], \quad (9)$$

which measures the ‘divergence’ between two $n \times n$ positive matrices R_1 and R_2 .

¹ We use real valued spherical harmonics.

3.2. A new SMICA configuration

In its regular mode of operation (as used in the Planck analysis, for instance), the SMICA method has two main ingredients: a semi-blind model $R_\ell(\theta)$ for the expected value of the spectra in \hat{R}_ℓ and a fitting criterion quantifying the discrepancy between \hat{R}_ℓ and $R_\ell(\theta)$. As discussed next, both these ingredients need to be adjusted for the present work, which addresses small scales limitations of the CMB angular power spectrum estimation, such as noise and point sources.

3.2.1. Data splits

The angular power spectra of sky maps always contain a noise term which needs to be accurately characterized in order to avoid bias, especially at small scales. Characterization of noise is often not trivial. Noise derives from the instrumental measurement and processing chain, making its properties difficult to establish. One possibility is to compare the noise contribution in data splits. These splits are obtained by dividing in two halves the time-ordered data sequences. For sky maps, this consists in generating the map with just half of the time ordered information. Therefore each data split contains the same astrophysical signal, but has a different noise contribution.

In practice this means that the observations leading to $\mathbf{y}_{\ell m}$ are split in two parts and processed independently, yielding two sky maps and therefore two sets $\mathbf{y}_{\ell m}^a$ and $\mathbf{y}_{\ell m}^b$ of harmonic coefficients such that:

$$\mathbf{y}_{\ell m}^a = \mathbf{o}_{\ell m} + \mathbf{n}_{\ell m}^a \quad \text{and} \quad \mathbf{y}_{\ell m}^b = \mathbf{o}_{\ell m} + \mathbf{n}_{\ell m}^b, \quad (10)$$

where the noise coefficients $\mathbf{n}_{\ell m}^a$ and $\mathbf{n}_{\ell m}^b$ are assumed to be uncorrelated. In the typical and simplest case of a balanced data split, one has:

$$\mathbf{y}_{\ell m} = \frac{1}{2} (\mathbf{y}_{\ell m}^a + \mathbf{y}_{\ell m}^b) = \mathbf{o}_{\ell m} + \frac{1}{2} (\mathbf{n}_{\ell m}^a + \mathbf{n}_{\ell m}^b) = \mathbf{o}_{\ell m} + \mathbf{n}_{\ell m}. \quad (11)$$

The regular SMICA method uses as input spectral covariance matrices defined as in Eq. (6). In this work, we consider using instead special matrices defined by:

$$\hat{R}_\ell^{\text{split}} = \frac{1}{2\ell + 1} \sum_m \frac{1}{2} (\mathbf{y}_{\ell m}^a \mathbf{y}_{\ell m}^{bT} + \mathbf{y}_{\ell m}^b \mathbf{y}_{\ell m}^{aT}), \quad (12)$$

where the sum of the two terms is necessary in order to symmetrize the matrix. On average $\hat{R}_\ell^{\text{split}}$ represents correctly the sky, but we need to take into account its statistical properties. The first term of Eq. (12) can be expanded as:

$$\frac{1}{2\ell + 1} \sum_m \mathbf{y}_{\ell m}^a \mathbf{y}_{\ell m}^{bT} = \frac{1}{2\ell + 1} \sum_m (\mathbf{o}_{\ell m}^a \mathbf{o}_{\ell m}^{bT} + \mathbf{o}_{\ell m}^a \mathbf{n}_{\ell m}^{bT} + \mathbf{n}_{\ell m}^a \mathbf{o}_{\ell m}^{bT} + \mathbf{n}_{\ell m}^a \mathbf{n}_{\ell m}^{bT}), \quad (13)$$

By construction, these matrices contain only correlations between maps with independent noise realizations and therefore they have a zero-mean noise contribution. More specifically, if we denote $\langle \cdot \rangle_N$ the average over noise realisations, one has:

$$\langle \hat{R}_\ell \rangle_N = \widehat{O}_\ell + N_\ell \quad \text{but} \quad \langle \hat{R}_\ell^{\text{split}} \rangle_N = \widehat{O}_\ell, \quad (14)$$

where the sky part contribution (not averaged over) is:

$$\widehat{O}_\ell = \frac{1}{2\ell + 1} \sum_m \mathbf{o}_{\ell m} \mathbf{o}_{\ell m}^T, \quad (15)$$

and where N_ℓ is the diagonal matrix with the noise spectra on its diagonal. The last three terms of Eq. (13) are zero on average, but not for a single realisation. In practice, there are chance correlations between the CMB and noise, which contribute to the scatter of the $\hat{R}_\ell^{\text{split}}$ matrix. So we need to take into account the fact that for a single realisation of the data, matrix $\hat{R}_\ell^{\text{split}}$ is not distributed as \hat{R}_ℓ or even as $\hat{R}_\ell - N_\ell$. How the noise-unbiased spectra contained in matrices $\hat{R}_\ell^{\text{split}}$ are jointly statistically fitted in the SMICA approach is described in next section.

3.2.2. Spectral matching criterion using data splits

We now consider using the SMICA criterion with the noise-unbiased spectral statistics $\hat{R}_\ell^{\text{split}}$. Let us denote $O_\ell(\theta)$ the expected value of $\hat{R}_\ell^{\text{split}}$ since this is also the expected value of \widehat{O}_ℓ . It would be naive to adjust the spectral model $O_\ell(\theta)$ by minimizing $\phi(\theta) = \sum_\ell (2\ell + 1)K(\hat{R}_\ell^{\text{split}}, O_\ell(\theta))$. To see that, consider the divergence between two matrices which are close to each other. The second order (quadratic) approximation of the divergence is:

$$K(R, R + \delta R) \approx K(R + \delta R, R) \approx \text{trace}(\delta R R^{-1} \delta R R^{-1})/4, \quad (16)$$

and it shows that the Gaussian likelihood penalizes the (small) deviations δR between covariance matrices through the inverse matrix R^{-1} . This is the proper weight (according to the maximum likelihood principle) to take into account the statistical variability in sample covariance matrices. Hence, if we were to use $K(\hat{R}_\ell^{\text{split}}, O_\ell(\theta))$, the statistical weight would not take into account the variability due to presence of the noise in the spectra. In order to account for that variability, we use an ansatz and minimize:

$$\phi^{\text{split}}(\theta) = \sum_\ell (2\ell + 1)K(\hat{R}_\ell^{\text{split}} + N_\ell^{\text{eff}}, O_\ell(\theta) + N_\ell^{\text{eff}}), \quad (17)$$

where N_ℓ^{eff} is a deterministic diagonal matrix containing the noise spectra which represents the effective noise contribution. Since it is introduced additively in both arguments of the $K(\cdot, \cdot)$, it should not introduce noise bias (see Eq. (16)).

In the standard SMICA configuration, the minimum $\phi(\theta)$ is of the order of the number of degrees of freedom d in the fit. We term this quantity ‘mismatch’. The mismatch is a diagnostic of the fit: high values indicate poor convergence or poor modeling. In this work we present a SMICA configuration based on data splits only, in which the statistical properties of the covariance matrices are only approximately represented by the model. In this case the recovered mismatch $\phi^{\text{split}}(\theta)$ for a converged fit is not $\sim d$, and its value is difficult to predict². Even though we do not have a predicted value, the mismatch is still an interesting quantity to look at, since very high values indicate that the model cannot represent the data complexity.

3.2.3. Semi-blind model

In the standard use of SMICA, a fully non-parametric model is used to model the foreground emission. We postulate that the sky emission can be represented in the harmonic domain by:

$$\mathbf{o}_{\ell m} = A \mathbf{s}_{\ell m}, \quad (18)$$

where A is a fixed (independent of ℓ) matrix of size $n \times (k + 1)$. Its first column, denoted \mathbf{a} , is the spectral energy distribution

² Nevertheless, for our configuration, simulations show that it is of the same order of magnitude of d .

(SED) of the CMB and the first entry of vector $\mathbf{s}_{\ell m}$ contains the CMB harmonic coefficients. The remaining k columns of matrix A (resp. the last k entries of $\mathbf{s}_{\ell m}$) represent foreground emissions. Since the CMB is statically independent from the foregrounds, one has:

$$O_\ell = \begin{bmatrix} \mathbf{a} & F \end{bmatrix} \begin{bmatrix} C_\ell^{\text{cmb}} & 0 \\ 0 & P_\ell \end{bmatrix} \begin{bmatrix} \mathbf{a} & F \end{bmatrix}^T, \quad (19)$$

where the $k \times k$ matrix P_ℓ is the covariance matrix of the foregrounds. The sources are modelled as Gaussian isotropic signals, since the only information retained is their angular power spectrum and their emission law in frequency. Even though this approximation does not hold for foregrounds, it does not affect CMB recovery as long as the emission law of CMB is well known (Cardoso 2017).

In the usual SMICA model, the $n \times k$ matrix F is unconstrained and the symmetric matrix P_ℓ is only constrained to be non-negative. This amounts to saying that foreground emission can be represented by k templates with arbitrary SEDs, arbitrary angular spectra and arbitrary correlation.

In this work, we shall consider a more constrained foreground model. Those constraints include forcing zero-terms in matrix P_ℓ (for instance to express independence between point source emission and Galactic emission) as well as imposing a spectral dependence to some entries (for instance flat angular spectra for point sources). This is discussed and detailed in next section.

3.3. Parametric models of foreground emission

A strength of the regular SMICA approach is that very little assumptions are made regarding the foreground emissions. In the case of Planck data analysis, it is safe to assume that the CMB has a black body emission law, within calibration errors. Nonetheless, nothing can be said about the other parameters: in an implementation as in Eq. (19), the foregrounds are described as a multidimensional component whose spectrum and emission law are totally free.

Some of the foreground emissions, in particular galactic emissions, present a degree of correlation that prevents their description as separate components. If two emissions are not independent, then ICA methods, on which SMICA is based, can not separate them. Thus all dependent emissions must be grouped in the analysis and considered as one single multidimensional component (Cardoso et al. 2008). In the case of the model in Eq. (19), all the foreground emissions are grouped in one single component P_ℓ . The existence of a correspondence between the spectra of this matrix with a given physical foreground emission is not guaranteed.

Large scale foregrounds, such as thermal dust, are well fit by multidimensional foregrounds, since the extra dimensions account for the spatial variability of the foreground emission and its eventual correlations with other foregrounds. Instead, small scale foregrounds, such as point sources, dominate in a region of the angular power spectrum where noise becomes important, are less favoured by the fit. When using a large multidimensional component these foregrounds may not be accounted for correctly. While this is less of an issue for the map reconstruction with SMICA, which aims at performing well at large scales (Planck Collaboration et al. 2016b,c), it can be a serious drawback when using the fit results for cosmological estimation, since separating the unresolved small scale foregrounds and the CMB power spectrum is difficult due to noise.

For this reason, as it is done in Patanchon et al. (2005); Planck

Collaboration XI et al. (2016), we parameterize the foreground model. In particular, in this work we use a semi-blind model, by enforcing some minimal constraints on the extragalactic contamination.

The main sources of foreground contamination at the frequencies of interest of this study are thermal dust, extragalactic shot noise and clustered contamination from point sources. As detailed in Sect. 2, the shot noise point sources emission can be divided into a radio and an infrared component. The clustered point source contamination instead, only originates from infrared galaxies. We build the foreground model as the sum of three uncorrelated components: a bidimensional component that accounts for dust and clustered CIB (cCIB), and two unidimensional components to account for unresolved radio and infrared point sources:

$$P_\ell = \begin{bmatrix} P_\ell^{dust+cCIB} & 0 & 0 \\ 0 & 0 & P_\ell^{rad} & 0 \\ 0 & 0 & 0 & P_\ell^{ir} \end{bmatrix}. \quad (20)$$

In practice, the clustered CIB is fitted together with thermal dust at 545 GHz and scaling this template to lower frequencies. The solid line represent the ND clustered CIB, obtained by separately fitting data points at each frequency. This model does not account for all the foreground contamination. In particular, both cCIB and dust present spatial variations in their spectral properties and would require more spectral dimensions. For point sources, we assume perfect coherence in frequency, which may not be true, but this would also require to describe them as multidimensional components (see for example Millea et al. (2012); Paoletti et al. (2012) for similar parameterizations of the extragalactic foregrounds). The dimensionality of the model is fixed by the number of observations, and including more frequency channels increases also the complexity of the foreground emission to describe. We thus find a balance between having enough observations to allow good separation and reducing foregrounds complexity.

In the present configuration it is not possible to disentangle the clustered CIB and dust. A more refined configuration, that includes a zone approach in SMICA and thus exploits the different spatial distributions of dust and clustered CIB, could in principle separate them. The interest of this, apart from studying the properties of dust and cCIB (Mak et al. 2017), is that it could improve the quality of the recovered CMB spectrum. The foreground contamination that is not accounted for by the model results in an increase of the final mismatch. However it is possible that a fraction of it projects on the CMB component. As we will see later, this can be checked with the aid of simulations.

The spectrum and emission law of dust and cCIB are freely fitted in each bin. Instead, we impose some constraints on the point sources part of the model, by making use of the physical knowledge we have. Their spectra are constrained to be flat, consistently with the prediction that the point sources can be modeled as shot noise. We expect that at the extrema of our frequency range only one population is clearly detected. This could induce the algorithm to find non-physical values for the emission law of the subdominant population. For this reason, we constrain the columns of the mixing matrix \mathbf{A} relative to point sources to take only positive values, by fitting at each frequency the exponent of an exponential. Apart from positivity, we make no further assumption on the emission law shape. This configuration allows us to recover the joint emission law of point sources. It is not possible to disentangle the emission of the two populations, since there is an intrinsic degeneracy between components

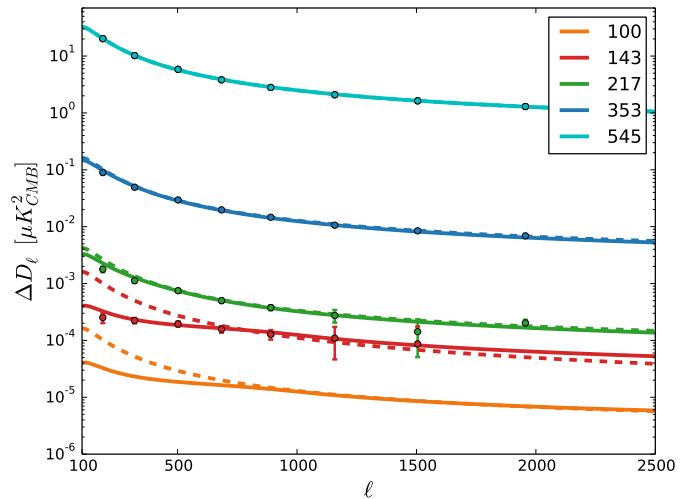


Fig. 1: Angular power auto-spectra of the clustered CIB component used in simulations. The dashed line represent the 1D clustered CIB spectra, obtained by fitting data points to a polynomial at 545 GHz and scaling this template to lower frequencies. The solid line represent the ND clustered CIB, obtained by separately fitting data points at each frequency. Overplotted data are taken from Table D2 in Planck Collaboration XXX et al. (2014). No data points are available for the 100 GHz clustered spectrum, which is taken to be one order of magnitude less than the 143 GHz clustered spectrum. Spectra have been corrected for shot noise contribution in order to match data points.

that have the same shape of the angular power spectrum (Delabrouille et al. 2003). For this reason, throughout the text we present results on the joint point sources emission.

The CMB angular power spectrum is freely fitted in each bin. Its emission law, with the calibration correction factors obtained by SMICA is instead fixed.

This refined model is more useful for a physical understanding of the foregrounds, and answers the issue stated above of separating the CMB and point sources, which dominate at scales where the noise becomes important and are thus difficult to characterize. Without a dedicated model for point sources, it is not possible to know what is their contribution to the total foreground level, hence it is not possible to correctly remove them from the CMB. In this sense point sources are degenerate with the CMB emission at small scales. We must note that the extra information gained on point sources comes at the cost of increasing the mismatch between the data and the proposed model with respect to an unconstrained model.

4. Data

In this analysis, we use both simulations and Planck 2015 half-mission data.

4.1. Simulations

In order to test our model, we construct simulations of sky observations at the frequencies of interest, which are a subset of the Planck HFI frequencies: 100, 143, 217, 353 and 545 GHz. For our main analysis we do not consider the 857 GHz channel, even though we also build simulations for this frequency: more details about this choice are given in Sect. 5.3. The astrophysical emissions we consider are the CMB, the thermal dust and

two extragalactic point sources populations, the radio and the infrared ones. For the latter, we simulate the clustered as well as the shot noise emission.

In order to better test our model with respect to extragalactic contamination, we produce three sets of simulations. They all contain CMB, dust, radio point sources, infrared point sources, clustered CIB and noise, but the properties of these signals differ in each set. We introduce here the general idea of the three different simulation sets. Technical details on how we build the different foreground components are given later. The three simulations sets are:

- SET1: these simulations have an idealised foreground content. All the foregrounds are simulated as a single template rigidly scaled through frequency. We refer to foregrounds of these simulations as 1D or unidimensional, since their contribution in all auto-spectra of sky maps can be described by a single angular power spectrum rescaled in frequency, and they present no decoherence in the cross-spectra. Values for the angular power spectra of point sources and the clustered CIB at $\ell = 3000$ are given in Table 1. The angular power spectra of the clustered CIB component are plotted in Fig. 1;
- SET2: these simulations include one foreground source with some frequency decoherence. Galactic dust and the two point source populations are simulated as a 1D template each, which is rigidly scaled through frequency (refer to Table 1 for point sources). The clustered CIB presents some frequency decoherence, i.e.:

$$C_{\ell}^{CIB \nu_1 \nu_2} = \alpha_{\nu_1 \nu_2} \sqrt{C_{\ell}^{CIB \nu_1} C_{\ell}^{CIB \nu_2}}, \quad (21)$$

where the coefficients $\alpha_{\nu_1 \nu_2} \leq 1$ are taken from Planck Collaboration XXX et al. (2014) and are reported in Table 2. The angular power spectrum shape is modeled on observational estimates: the shape of the angular power spectra at each frequency differ slightly. The power spectra at different frequencies are presented in Fig. 1. We refer to this CIB component as ND or multidimensional;

- SET3: these simulations have the most realistic foreground content. The two point source populations are simulated as a 1D template each, which is rigidly scaled through frequency (again refer to Table 1). The clustered CIB is simulated as in SET2. The dust component presents spectral index and dust temperature variability on the sky, using results from Planck Collaboration XLVIII et al. (2016). We refer to this dust component as ND or multidimensional.

These three sets are labeled SET1, SET2 and SET3 throughout this work. The SET2 and SET3 cases are studied since observations show that there could be a partial decoherence through frequency of the CIB emission (Planck Collaboration XXX et al. 2014, Sect.6.2), this effect being mostly evident at the two lowest frequencies 100 and 143 GHz. The third case also includes a realistic dust representation, which takes into account the inhomogeneous dust properties on the sky. Both are important tests since the SMICA method assumes no frequency decoherence or variability of the spectral index for the unidimensional sources: in the SMICA model this variability is accounted for as an increase of the dimensionality of the source. However the model has a maximum number of dimensions fixed by the number of observations.

In order to reproduce the Planck half-mission maps used in this analysis, for each simulation we produce 2 maps for each frequency, and each couple of maps at same frequency has identical astrophysical content but a different realization of

white Gaussian noise. We produce N=30 simulations for each set.

Building the components The CMB component is simulated from a theoretical CMB temperature angular power spectrum using the HEALPix tool (Górski et al. 2005). The power spectrum is obtained using the code CosmoMC, with the following set of input cosmological parameters: $H = 67.31$, $\tau = 0.078$, $\omega_b = 0.02222$, $\omega_c = 0.1197$, $n_s = 0.9655$, $\ln(10^{10} A_s) = 3.089$, $y_{He} = 0.24$ and $m_\nu = 0.06$ eV.

There are two different thermal dust components: one is a single template scaled through frequency (SET1 and SET2 simulations), while the other presents more complex features (SET3). The former, labeled “1D”, is the thermal dust map at 545 GHz delivered by the *Planck Collaboration* (Planck Collaboration X et al. 2016), which we choose in order to have a realistic spatial distribution. This template is scaled through frequency according to the grey-body law described by Eq. (2.1) with $T=19.4$ and $\beta=1.6$ (Planck Collaboration XLVIII et al. 2016). Note that this template is partially contaminated by residual CIB emission (Planck Collaboration X et al. 2016, Sect. 4), which makes the dust contribution of this template at high ℓ higher than the real dust contribution. This makes the fit of the high- ℓ components slightly more difficult for SMICA. Due to the fact that thermal dust and the clustered CIB have similar emission laws, the presence of a residual contamination of CIB in the small scales of the thermal dust template map is not to be excluded, i.e., the small scale power of this template could be higher than the real dust distribution. The latter, labeled “ND”, is simulated using the GNILC model maps for the spectral index β_d , the dust temperature, and the opacity, obtained as described in Planck Collaboration XLVIII et al. (2016). They are combined through Eq. (2.1) to produce a dust map at each ν .

For the extragalactic content, that is point sources and clustered CIB, we base ourselves on Planck Collaboration XXX et al. (2014), which provides estimates for the radio and infrared point sources shot noise levels, the angular power spectra of CIB emission and its decoherence coefficients at Planck frequencies. Shot-noise levels are given at all the frequencies of interest of this paper, and we therefore use them for point source simulations. We model the two point source populations as two realisations of shot noise maps, i.e., with a flat angular spectrum. The amplitudes of the shot noise power are taken from Table 6 and 7 in Planck Collaboration XXX et al. (2014) and are summarized in Table 1.

CIB spectra and decoherence coefficients are given by the Planck analysis for all frequencies except 100 GHz: we choose for this channel values one order of magnitude lower than the 143 GHz estimates. The CIB angular power spectra reported in Table D2 of Planck Collaboration XXX et al. (2014) contain both the clustered and shot-noise contribution: the latter is subtracted to obtain clustered CIB templates.

To produce the clustered CIB component maps at each frequency we compute the covariance matrix R_{ℓ}^{CIB} of CIB auto- and cross-angular power spectra. More specifically:

- for SET1, i.e., the 1D clustered CIB, we fit a polynomial to the data points of the 545 GHz power spectrum, and all the other auto- and cross-spectra are obtained by scaling this template. Scaling coefficients for auto-spectra are obtained from Planck Collaboration XXX et al. (2014), while for cross-spectra we use Eq. (21) with $\alpha_{\nu_1 \nu_2} = 1$. $C_{\ell=3000}$ values are reported in Table 1;

Table 1: Simulation parameters for point sources and clustered CIB as $C_{\ell=3000}$ levels in Jy^2/sr .

	Radio Point Sources	IR Point Sources	1D clustered CIB
100	8.48	0.150	0.136
143	6.05	1.20	3.43
217	3.12	16.0	14.4
353	3.28	225	209
545	2.86	1454	1550
857	4.28	5628	5397

Table 2: Decoherence coefficients for the ND clustered CIB.

	100	143	217	353	545	857
100	1	-	-	-	-	-
143	0.99	1	-	-	-	-
217	0.78	0.78	1	-	-	-
353	0.54	0.54	0.91	1	-	-
545	0.51	0.51	0.90	0.983	1	-
857	0.45	0.45	0.85	0.911	0.949	1

- for SET2 and SET3, i.e., the ND clustered CIB, at each frequency we fit a polynomial to the data points of the auto-spectra given in [Planck Collaboration XXX et al. \(2014\)](#), and we extrapolate to higher ℓ when necessary. Only the auto-spectra are used, while cross-spectra are derived via Eq. (21). The decoherence coefficients of angular power spectra between different frequencies are detailed in Table 2.

The auto-spectra for both cases are presented in Fig. 1. Once the covariance matrix R_{ℓ}^{CIB} is constructed, the procedure for obtaining spherical harmonics is the same for both cases. We build the vector $\mathbf{x}_{\ell m}$, whose entries $x_{\ell m}^i$ are sets of spherical harmonics coefficients drawn from the normal distribution,

$$x_{\ell m}^i \sim \mathcal{N}(0, 1), \quad (22)$$

where $i = 1, 2, \dots, N$, and N is the number of frequencies we use. We then obtain spherical harmonics for the CIB as:

$$x_{\ell m}^{CIB} = Z_{\ell}^{CIB} \mathbf{x}_{\ell m} \quad (23)$$

where Z_{ℓ}^{CIB} is the square root of the clustered CIB covariance matrix $R_{\ell}^{CIB} = Z_{\ell}^{CIB} Z_{\ell}^{CIB}$.

In order to build simulations, the CMB and foregrounds maps are added with their respective amplitude for each frequency and then smoothed with their respective beam window function³. By construction, there is no correlation between the foregrounds and the CMB.

The instrumental noise is simulated at the map level as white Gaussian noise. Noise amplitudes are determined using Planck noise simulations as provided at NERSC⁴.

4.2. Planck data

We use data maps from the 2015 full Planck release and we select the two half-mission maps at each frequency between 100 and 545 GHz. Half-mission maps are data split obtained by dividing the full mission time-ordered data into two halves. The maps are degraded to a lower resolution of $N_{\text{side}} = 1024$ using *HEALPix*.

³ provided in Planck's RIMO, which can be downloaded from the *Planck Legacy Archive* <http://pla.esac.esa.int/pla/>

⁴ <http://crd.lbl.gov/cmb-data>

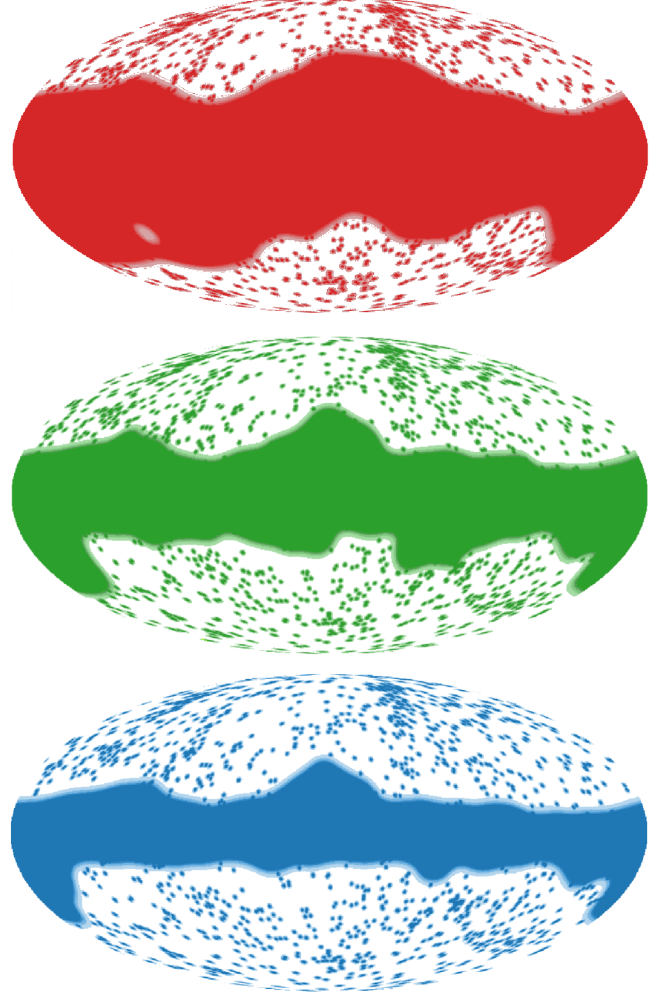


Fig. 2: Apodised masks used in this analysis. The retained sky fractions $f_{\text{sky}}=0.3, 0.5, 0.6$ are shown in red, green and blue respectively. The shaded region is the apodised part.

4.3. Masks and binning

In order to reduce the foreground contamination, the central regions of the sky are masked. Masks are produced as a sum of a galactic and a point source part. We use a set of three masks with the same point source masking but different galactic coverage. The masks used are shown in Fig. 2 and have effective $f_{\text{sky}} = 0.3, 0.5, 0.6$. More details on the masks preparation are given in Appendix A.

Since SMICA works with spectral covariance matrices, angular power spectra between all couples of maps are calculated with the *PolSpice* (Chon et al. 2004) package. Using the *Pol-*

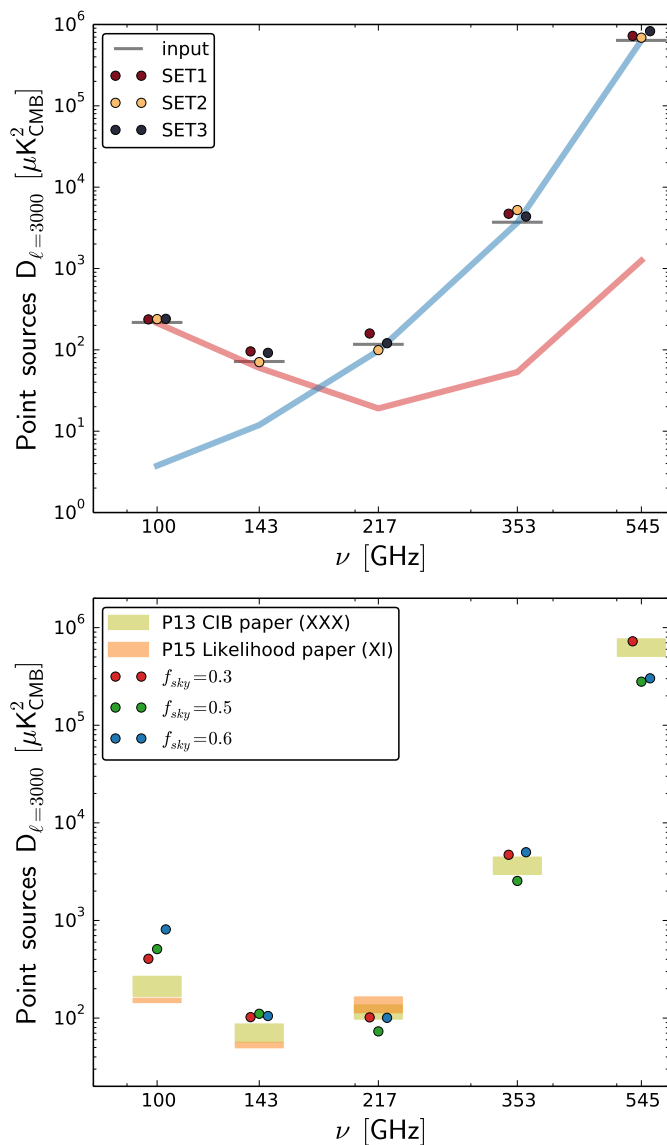


Fig. 3: Combined (infrared and radio) shot noise point sources D_{ℓ} power at $\ell = 3000$ obtained from the fit. *Top panel*: simulations average of point sources at $f_{\text{sky}} = 0.5$, shown in dark red for SET1 simulations, yellow for SET2 and black for SET3. The red and blue band show the simulations input for the radio and infrared point sources respectively, while the grey horizontal line at each ν represents the joint point source input. *Bottom panel*: point sources for the three different masks of $f_{\text{sky}} = 0.6, 0.5, 0.3$ in blue, green and red respectively. The yellow and orange bands represent the expected shot noise point source contribution estimated in Planck Collaboration XXX et al. (2014) and Planck Collaboration XI et al. (2016), where the width of the coloured band represents the error on the expected value. Planck Collaboration XI et al. (2016) gives expected values for the three low ν channels only.

Spice routine, we correct the resulting power spectra for the point spread function of the instrument using the beam window functions provided by the full Planck release³, for the pixel window function and for the mask leakage. All the angular power spectra are binned uniformly with $\Delta\ell = 15$. With these spectra, and following the procedure detailed in Sect. 3.2.1, we build at

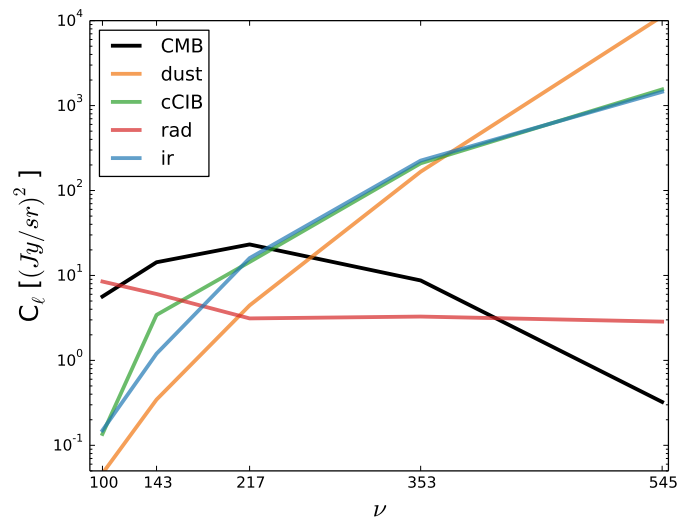


Fig. 4: Input spectral behaviour of dust, clustered CIB, infrared and radio point sources of SET1 simulations at $f_{\text{sky}} = 0.5$, plotted as $C_{\ell=3000}$. Radio and infrared point sources are labeled “rad” and “ir” respectively. Infrared point sources, cCIB and dust, plotted in blue, green and orange respectively, present similar emission laws. CMB black-body emission law, which is not fitted for, is plotted in black.

each bin a 5×5 covariance matrix $\hat{R}_{\ell}^{\text{split}}$. We work on the range $\ell = [100, 2500]$: we neglect in this analysis the large angular scales $\ell < 100$, where dust has complex features that can not be described by a bidimensional component. Also, we limit our analysis around $\ell \sim 2500$, since for higher multipoles noise becomes dominant.

The Planck maps are slightly decalibrated among each other. Similarly to what is done in the Planck analysis (Planck Collaboration XII 2014), we perform a dedicated free fit in the multipole range of the first and second peak to recover calibration factors. We use relative calibration correction factors with respect to 143 GHz: $y_{\text{cal}} = [1.00079, 1., 1.0029, 1.008, 1.0174]$ for the five channels between 100 and 545 GHz.

5. Testing the method

We detail here the analysis and fitting procedure to obtain the CMB power spectrum. We test this method on simulations first and Planck 2015 temperature data then. The spectra recovered from simulations and data are used to estimate cosmological parameters, which are presented in Sect. 6.

5.1. Simulations analysis

While the simulated foregrounds can not reproduce the full complexity of real data foregrounds, a study on simulations is a good test for understanding to which degree we can recover the point source signal and the CMB angular power spectrum. We process the three simulation sets with the foreground model described by Eq. (20). For SET1, since foregrounds are all 1D, we constrain the $P_{\ell}^{\text{dust+cCIB}}$ component to be diagonal.

In the top panel of Fig. 3 we show the recovered shot noise point source signal for the average of all simulations of each set at $f_{\text{sky}} = 0.5$.

We show results for the intermediate f_{sky} value, but we observe no mask dependence in the recovered point source emission. We

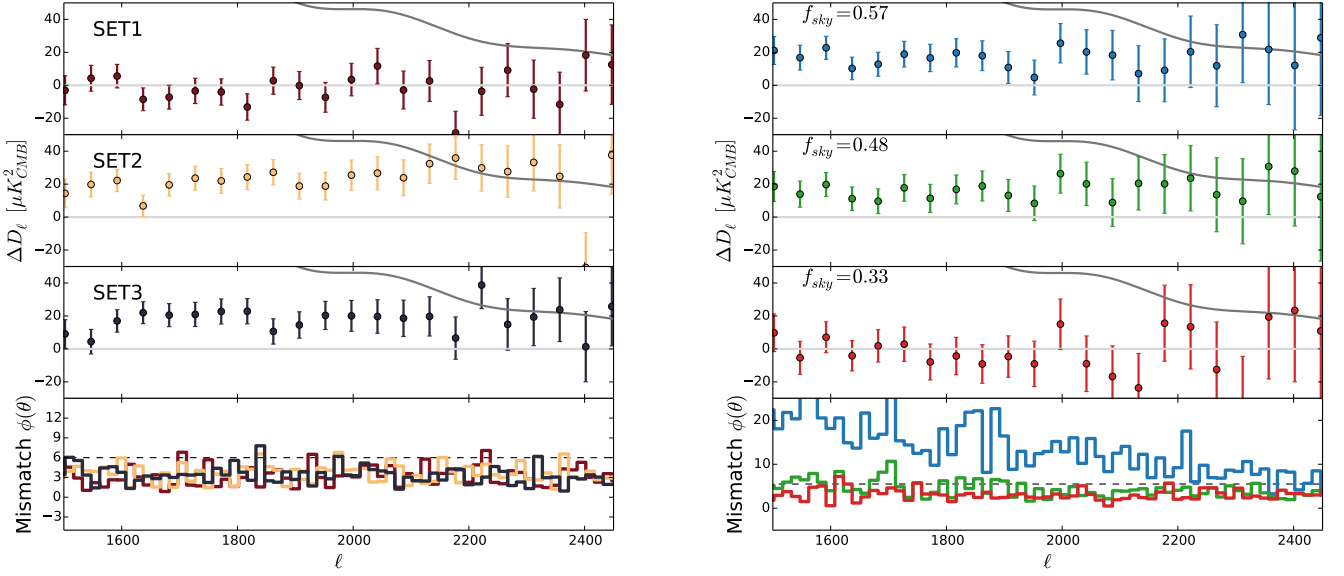


Fig. 5: Top three panels show the residuals in D_ℓ between the fit results and the theoretical CMB power spectrum. Dark grey line shows the theoretical CMB spectrum downscaled by a factor 0.2 for readability. Bottom panel shows the mismatch between the model and the data after the fit as defined by Eq. (3.1) and the thin dashed line shows the expected mismatch per bin. Only one point every three bins is displayed. *Left panel*: Filled dots show differences between CMB spectra obtained from fit on simulations with respect to input CMB spectrum at each bin, at $f_{\text{sky}} = 0.5$, shown in dark red for SET1, yellow for SET2 and black for SET3. *Right panel*: Filled dots show differences between CMB spectra obtained from the fit on Planck 2015 half-mission data with respect to the Planck best fit Λ CDM Plik spectrum.

observe that the model is capable of recovering closely, up to small offsets, the point sources input for all the 3 cases. The SET1 case, which has all 1D foregrounds and is therefore an “ideal” test case for SMICA, presents a small offset in the three central frequencies. This is not surprising: even though the foreground content corresponds exactly to the SMICA model, the clustered CIB, the infrared shot-noise and the galactic dust have similar emission laws, and the corresponding columns of the matrix A are almost proportional, as seen in Fig. 4. This is far from ideal for ICA methods, since it limits the identifiability of the sources. Due to this we expect an exchange in power between dust, cCIB and infrared point sources. The offsets in SET2 and SET3 simulations are instead likely due to the fact that the model is incapable of representing the foregrounds complexity due to its limited dimensionality.

In the left panel of Fig. 5 we show residuals of the high- ℓ tail of the fitted CMB angular power spectrum with respect to the theoretical input. As seen from this Figure, the residual is at most one fifth of the CMB power at $\ell \geq 2200$. A residual contamination is present on average for the SET2 and SET3 cases only. The mis-evaluation of the clustered CIB contamination can be one source of bias in the CMB power spectrum estimation. The SMICA method assumes full correlation of all components through frequency. A partial decoherence of a component, as for example in SET2 for the clustered CIB, means that its spectral behaviour must be described by a multidimensional component. For galactic dust and clustered CIB, we have a 2D component describing both of them at the same time. While angular power spectra are fitted in each bin, the mixing matrix A is global: galactic dust and clustered CIB emissions, which are important at low and high multipoles respectively, compete for the columns of this matrix. As a consequence, complex features in these two emissions can not be fully accounted for. We expect that a part of the CIB and dust contamination projects onto the CMB, resulting in an offset

with respect to the input spectrum, as shown in the left panel of Fig. 5.

We can see that such a contamination is not detectable as a considerable increase in the mismatch, while it is clearly visible in the CMB residuals. Results in Fig. 5 are presented for $f_{\text{sky}} = 0.5$, but no significant trend with sky fraction is visible in most simulations. We see that the observed mismatch is lower than the expected value. This happens because of the peculiar statistical properties of the empirical covariance matrices used in this work, as described in Sect. 3.2.1. The value of the mismatch does not correspond to the number of degrees of freedom ν , which we plot anyway as a visual reference of the order of magnitude of the expected mismatch (see Sect. 3.2.2 for more details).

5.2. Data analysis

We fit a model as described in Section 3.3. The obtained CMB angular power spectrum is presented in Fig. 6 for the three different masks, while right panel of Fig. 5 shows residuals with respect to the reference CMB Planck spectrum at high- ℓ . The reference Planck spectrum is the theoretical Λ CDM spectrum obtained from best fit parameters of the Planck 2015 Plik likelihood exploration. Error bars are derived with the Fisher matrix. We observe in Fig. 5 that the results obtained for the CMB are in good agreement between the three different masks. We can see an increasing level of residual contamination, for increasing sky fraction. While this trend is not seen in simulations, we expect such a behaviour in real data since the foreground complexity increases. As observed in simulations, we expect that the model cannot fully capture dust and cCIB emission. Also, our simulations contain two point source populations perfectly correlated through frequency. While this is a good approximation, it might not represent the full extent of contamination produced by background galaxies. Another problem is the similar emission law

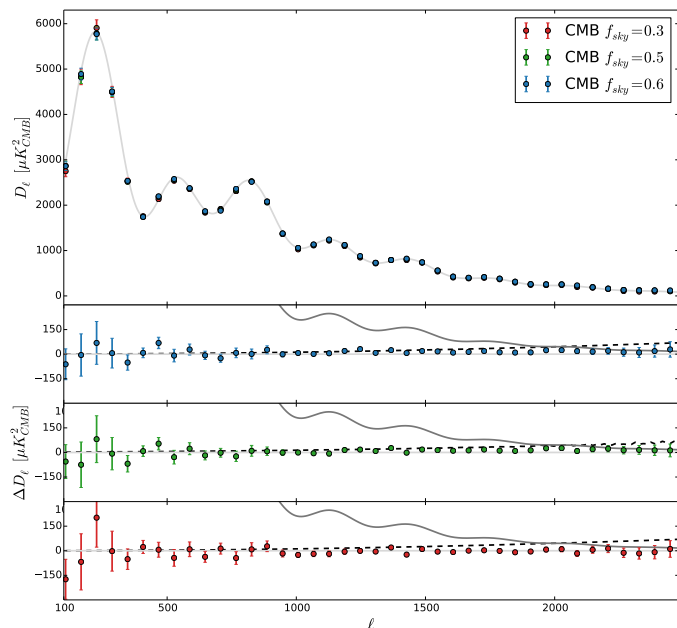


Fig. 6: CMB angular power spectrum obtained from the SMICA fit of the model to the three different data sets used, corresponding to the masks with $f_{\text{sky}} = 0.3, 0.5, 0.6$ (top panel). In grey we show the best fit theoretical Λ CDM spectrum obtained with Plik. Three bottom panels show the residuals between theory and data for the three cases, together with the theoretical value of the angular power spectrum scaled to 20% power in grey. The black dashed line shows the total contribution of extragalactic foregrounds at 217 GHz. To enhance readability, only one point in four is plotted.

between dust and CIB, which cannot be fully captured by the model; due to this, a fraction of the foreground contamination projects on the CMB and on the mismatch between the model and the data. We see that the mismatch is much higher than the mismatch found in simulations, in particular for the smallest mask and at low multipoles, where the thermal dust behaviour becomes more complex.

In the bottom panel of Fig. 3 we show the recovered point sources amplitudes for the three masks at $\ell = 3000$. Results for $f_{\text{sky}} = 0.3, 0.5$ are in good agreement with each other and with the expected amplitude as estimated by the *Planck Collaboration*. The $f_{\text{sky}} = 0.6$ results show an offset at the highest and lowest frequencies: again the model fails to fully represent the foregrounds complexity. We expect point sources estimates at smaller f_{sky} to be more accurate, since the galactic contamination is lower. The offset of point source emission law is related to the offset in the CMB power spectrum, but cannot fully explain it. Forcing point sources emission law to the result obtained for the largest mask, i.e., to a value closer to the expected one, reduces only slightly the mismatch and the CMB bias.

5.3. Using 857 GHz

The number of channels used is directly related to the dimensionality of the foreground model. Including more observations allows for a higher dimension, but also adds new features in the data which need to be described. We choose to exclude low frequency observations from our analysis since this would include synchrotron and free-free emission and thus increase the Galac-

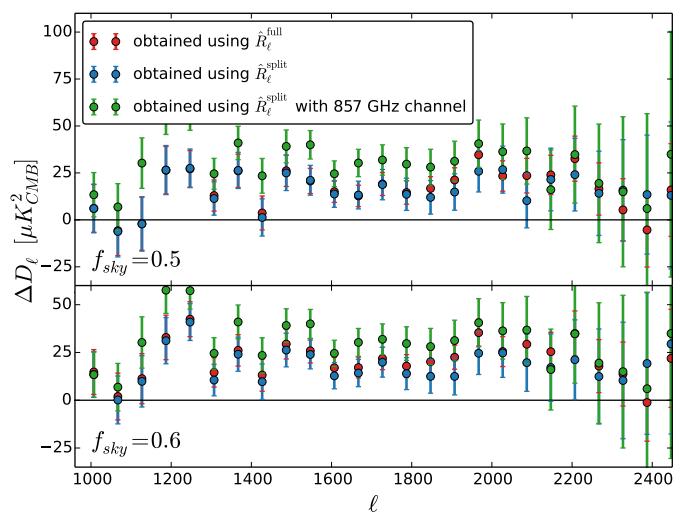


Fig. 7: CMB angular power spectrum D_ℓ residuals with respect to Planck theoretical best fit spectrum for three different SMICA configurations. In blue we show the leading configuration of this paper using cross-spectra of data splits, in red the one using cross- and auto-spectra as described in Sect. 5.4 and in green the results obtained including 857 GHz channel observations, as detailed in Sect. 5.3. Only one point every three bins is displayed. We show results for $f_{\text{sky}} = 0.5$ in the top panel and $f_{\text{sky}} = 0.6$ in the bottom panel. We note that the case which uses $\hat{R}_\ell^{\text{split}}$ without the 857 GHz channel has an overall smaller residual with respect to the other two cases.

tic foreground complexity. We also choose to exclude WMAP 94 GHz observations since they have a lower resolution than Planck data and this would oblige us to use a smaller ℓ range.

Higher frequency observations could in principle be useful since they contain mainly dust, infrared point sources and clustered CIB. However frequency decoherence of foregrounds makes the effective impact of high frequency channels negligible. We present in this section results on SET3 simulations and Planck data when adding the 857 GHz channel. For the analysis on data, the masks are adapted by adding point sources detected in the 857 GHz maps, but effective sky fractions are substantially unchanged. The fitting procedure is the same as described in Sect. 5.1 and Sect. 5.2, with the only difference that the $P_\ell^{\text{dust+CIB}}$ part of the model in Eq. (20) has now three dimensions instead of two.

For simulations we see no evident difference in the SMICA fit between adding or not the 857 GHz channels. For data, the CMB power spectrum for $f_{\text{sky}} = 0.5, 0.6$ is shown in Fig. 7. No improvement is seen with respect to the fit without the 857 GHz channel. While simulations show a good agreement between masks, the recovered point sources emission laws show an evident bias at low frequencies $\nu \leq 217$ GHz. This hints that a degree of decoherence is present between 857 GHz and lower frequencies shot noise emission. The mixing matrix columns reserved to point sources can not accommodate for both high and low frequencies, sacrificing the latter.

5.4. Without data-splits

The configuration described in Sect. 3.2.1 tests covariance matrices built using data split cross-spectra only. A simpler configuration would be to use the full $2N \times 2N$ covariance matrix of auto-

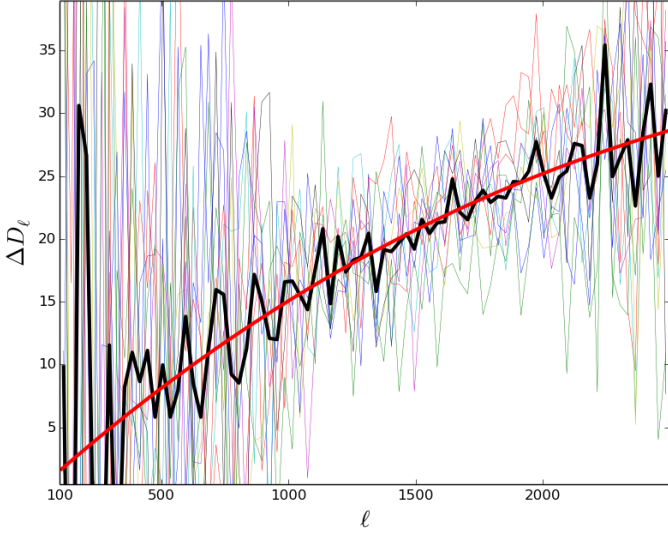


Fig. 8: Difference between SMICA best fit and input maps CMB angular power spectra for 10 SET3 simulations. The average of the differences is plotted in black, while the chosen template for the likelihood is plotted in red.

and cross-spectra, where N is the number of frequency channels. This matrix is defined as:

$$\hat{R}_\ell^{\text{full}} = \frac{1}{2\ell + 1} \sum_m \mathbf{y}_{\ell,m}^{\text{full}} \mathbf{y}_{\ell,m}^{\text{full}T}, \quad (24)$$

where $\mathbf{y}_{\ell,m}^{\text{full}} = [\mathbf{y}_{\ell,m}^a, \mathbf{y}_{\ell,m}^b]$. The model used in this case is:

$$R_\ell(\theta) = \begin{bmatrix} \mathbf{a} & F \\ 0 & P_\ell \end{bmatrix} \begin{bmatrix} C_\ell^{\text{cmb}} & 0 \\ 0 & P_\ell \end{bmatrix} \begin{bmatrix} \mathbf{a} & F \end{bmatrix}^T + N_\ell \quad (25)$$

where N_ℓ is the diagonal matrix containing the noise power spectra. In this configuration the noise power spectra are part of the fitted parameters. This higher number of parameters to fit is compensated by the increased dimension of the data matrix \hat{R}_ℓ .

On Planck data, we show in Fig. 7 that residuals for the cross-spectra only covariances \hat{R}_ℓ are lower than those obtained using the auto- and cross-spectra covariances $\hat{R}_\ell^{\text{full}}$. We attribute this difference to the higher number of parameters to fit in the full matrix case. Also, an error in the noise estimation reflects on the astrophysical part of the fit, and potentially on the CMB. Instead, in the configuration chosen for this study, noise spectra are known by construction and are not fit for, and thus they can not bias the fit. The drawback in this case is that the estimated error bars depend on the noise ansatz (see Sect. 3.2.2).

6. Cosmological parameters

We test our approach by obtaining cosmological parameters from the SMICA best fit angular power spectrum. We do this both on Planck data and on a subset of simulations. We compare the parameters obtained from simulations to the input ones. The parameters obtained from Planck data are compared to the baseline Planck 2015 results. Since we have only temperature data, we use a Gaussian prior on the parameter τ : this configuration in Planck Collaboration XI et al. (2016) is referred to as *PlikTT+tauprior*. For each case studied, we run Monte Carlo Markov Chains (MCMC) with CosmoMC (Lewis & Bridle 2002) in combination with PICO⁵ (Fendt & Wandelt 2007).

⁵ available for download at <https://github.com/marius311/pypico>

We also cross-check some of our runs using CosmoMC with CAMB (Lewis & Bridle 2002), and using CosmoSlik (Millea 2017) with PICO: we observe that results are consistent with those obtained using CosmoMC with PICO. For this reason, all the results presented in this analysis are obtained using the latter configuration.

6.1. The likelihood

We build our likelihoods from the best fit CMB spectra obtained from the SMICA fit for the different cases under analysis. We use an idealised form for the likelihood, which considers no intermode correlations. This approximation should not strongly affect our results since we use bins of $\Delta\ell = 15$. The likelihood takes the form:

$$-\ln \mathcal{L}(\hat{C}|C(\theta)) = \frac{1}{2}(\hat{C} - C(\theta)) \Sigma^{-1} (\hat{C} - C(\theta)) + c \quad (26)$$

where \hat{C} and $C(\theta)$ are the best fit and theoretical angular power spectra respectively, Σ is the covariance matrix given by the SMICA error bars on the best fit and c is a constant. The error bars are an estimate derived from the Fisher matrix. They represent the cosmic variance, foregrounds, noise and mask contribution to the error budget, but do not include uncertainties on calibration and beams.

We explore a minimal Λ CDM model with two approximately massless neutrinos and one massive neutrino with $\sum m_\nu = 0.06$ eV. We also use a Gaussian prior on the optical depth to reionization: for the MCMC on data we use $\tau = 0.07 \pm 0.02$, the same as in Planck analysis (Planck Collaboration XI et al. 2016), while for simulations we choose $\tau = 0.078 \pm 0.02$, since $\tau = 0.078$ corresponds to the input value of the simulated CMB maps.

There is a small amount of foreground residuals in the CMB spectra, as evident from Fig. 5. This residual has to be accounted for in the likelihood formulation with a nuisance model. Finding a shape for the foreground residuals is not trivial, since nuisance parameters can bias the cosmological parameters when incorrectly chosen. We opt for a physical modeling of the nuisance parameters based on our foreground knowledge. Paoletti et al. (2012) find that two terms for the shot noise and clustered contribution suffice to account for the background galaxies contribution. Also, we need to account for residuals of the galactic dust. We do not consider any term for the SZ residual contamination. The Planck Collaboration derives cosmological parameters from the CMB maps, including the SMICA one (Planck Collaboration IX et al. 2016). The SMICA map cosmological parameters cannot be directly compared to this analysis parameters since the map-making procedure can add some foreground contribution, thus we compare our results with those obtained with the Planck likelihood, which uses angular power spectra of data maps. Nevertheless, similarly to what it is done in the Planck analysis on CMB maps, we use a nuisance model that comprises:

- a point source term with flat spectrum. Its amplitude is regulated by the parameter A^{PS} , which corresponds to the point sources contribution for $D_{\ell=3000}$;
- a clustered CIB term with a spectrum $\ell^{n_{CIB}}$. We fix $n_{CIB} = -1.3$ for most explorations, unless otherwise stated. The amplitude A^{CIB} represents the CIB contribution for $D_{\ell=3000}$;
- a dust term with an angular power spectrum $\ell^{-2.6}$. The nuisance parameter A^{dust} is defined as the emission for $C_{\ell=500}$.

The physical nuisance model is our reference configuration. In a subset of cases we also test using a smaller number of nuisance

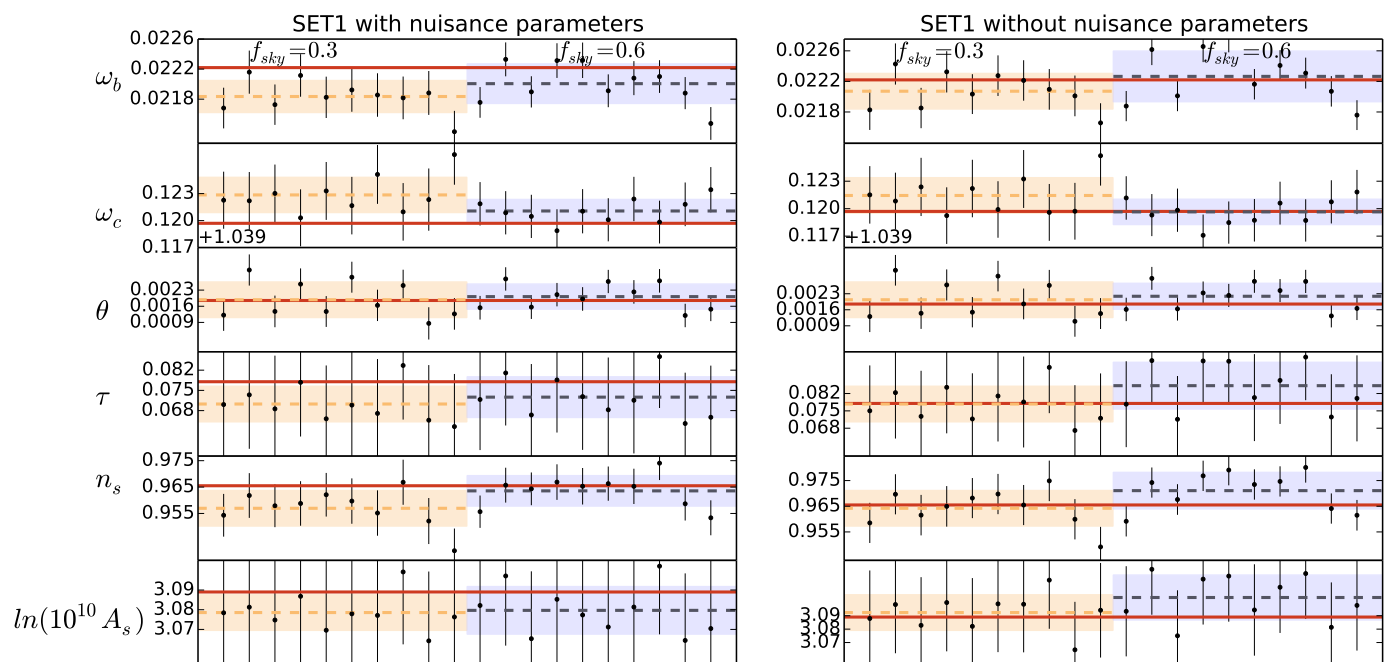


Fig. 9: Cosmological parameters for a subset of 10 simulation of SET1 with (left) and without (right) a model for nuisance parameters in the likelihood. Results are presented for $f_{sky}=0.3$ in yellow and $f_{sky}=0.6$ in blue. For each f_{sky} , the dashed line represents the average of the simulations marginal means and the shaded band represents the 1σ scatter around this average. Each dot represents the marginal mean and 68% CL error bar of the parameters in a given simulation. The red line shows the input parameters of theoretical C_ℓ used for simulations.

parameters, as well as the use of a single template derived from simulations. The template is based on the shape of the average foreground residuals in SET3 simulations at the largest f_{sky} , i.e., the case with the strongest residual contamination in the CMB spectrum. Its shape does not represent any particular foreground contamination, however it is very close to the clustered CIB theoretical shape, meaning that this is the major contribution that we expect in the residuals according to simulations. Fig. 8 shows the difference between the best fit CMB spectrum and the spectrum of the input CMB map for 10 SET3 simulations. The input maps are unmasked, thus the low- ℓ scatter is largely driven by cosmic variance. From these we compute the average residuals and fit a shape for the template. We use this template as a unique nuisance component in the likelihood exploration, only changing its amplitude.

6.2. Cosmological parameters from simulations

We explore cosmological parameters for the first 10 simulations of each set. For these simulations, we obtain parameters for both the largest and the smallest masks, to check for effects that depend on retained sky fraction. For each simulation and sky fraction, we use the best fit CMB angular power spectrum of SMICA to build a likelihood as described in the previous section. The main analysis is done using the physical parameterization of the nuisance model. The list of all parameters is detailed in the first column of Table 3. Cosmological parameters are presented in Fig. 9 for SET1 and Fig. 10 for SET2 and SET3, where the red line shows simulation inputs and the wide coloured band show 1σ scatter of the marginal mean values.

SET1 simulations are those that best recover the input CMB power spectrum in the SMICA fit, thus we expect their residual foreground content to be very low. We test SET1 simulations in

two different configurations, letting the nuisance parameters free and setting all of them to zero, i.e., not accounting for any residuals in the likelihood exploration. As shown in the right panel of Fig. 9, the MCMC exploration with nuisance parameters shows evident biases with both masks. As a cross-test, we obtain cosmological parameters from theoretical spectra to which we add some scatter according to the expected cosmic variance. In this case the average parameters obtained coincide with the input, meaning that the shift we observe in Fig. 9 are due to foreground residuals and not to our pipeline implementation.

As we will see in Sect. 6.3, there is a degeneracy between the shape of the foreground residuals and the cosmological parameters, and a wrong estimation of the nuisance parameters can induce biases. In particular, when we have a low f_{sky} , the error bars are larger and we can more easily mix up the CMB and the foregrounds. This is evident in Fig. 9, which shows how most biases are strongly reduced when nuisance parameters are removed, especially for $f_{sky} = 0.3$, where we expect to have the lowest, and thus most degenerate, residuals. Due to the low level of residuals in the CMB spectra, the nuisance parameters are not well estimated and are in most cases compatible with zero. A level of residuals is present in the data, but since this is not well determined, it is not correctly accounted for.

For SET2 and SET3 simulations we obtain less biased results: in Fig. 10 we can see that biases of parameters are less evident, especially for the SET3 case. In this case we did not run the nuisance-free likelihood given that the level of foreground residuals is too high to justify such a test. Since the level of residuals in these simulations is higher than in SET1, it is better constrained in the parameters exploration. We observe very small changes with sky fraction, the most relevant one being the decrease in size of the 1σ scatter band with increasing f_{sky} , as expected. We note that marginal errors on τ and A_s for individ-

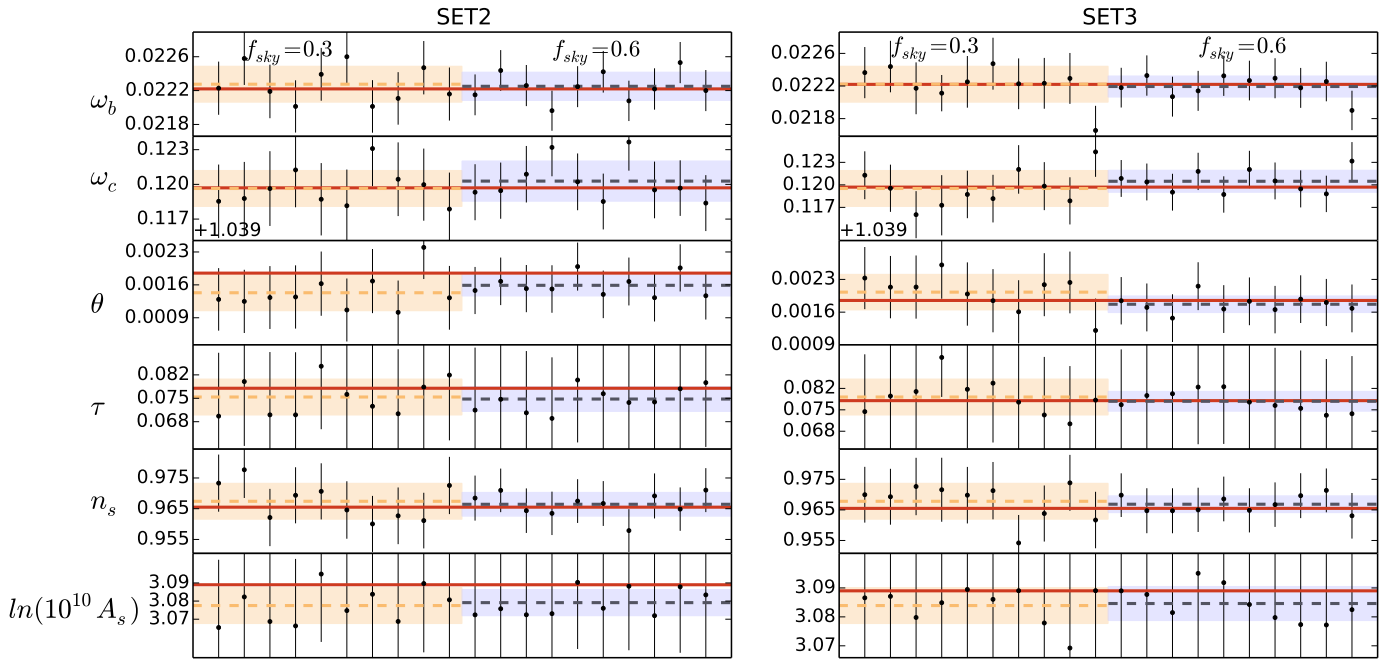


Fig. 10: Cosmological parameters for a subset of 10 simulation of SET2 (left) and SET3 (right). Results are presented for $f_{sky}=0.3$ in yellow $f_{sky}=0.6$ in blue. For each f_{sky} , the dashed line represents the average of the simulations marginal means and the shaded band represents the 1σ scatter around this average. Each dot represents the marginal mean and 68% CL error bar of the parameters in a given simulation. The red line is the input of theoretical C_ℓ used for simulations.

ual simulations are quite large, while the scatter of the mean is not: this is not surprising since the marginal error on τ , and consequently on A_s , is regulated by the Gaussian prior $\tau = 0.07 \pm 0.02$ we impose.

Since the nuisance parameters are not well constrained, a model for the residuals with less parameters could in principle reduce the uncertainty in the exploration. For the SET3 case only, we test the template configuration of the likelihood described in the previous section. In this configuration only one nuisance parameters is fitted, which is the amplitude of the template. In terms of biases, the results are equivalent to those obtained with the physical nuisance model. The only relevant change is that the discrepancy on A_s is reduced, while that on ω_b is increased. This suggests that the average foreground contamination represented by the template does not fully describe the details of the residuals in each CMB spectrum of simulations, and that the details of foreground modeling in the likelihood are important for accurate estimation of cosmological parameters.

6.3. Cosmological parameters from Planck data

We build a likelihood for each mask from best fit spectra obtained from the analysis detailed in Sect. 5.2. We call these three likelihoods Like-F03, Like-F05 and Like-F06, where FX refers to the f_{sky} of the mask used. We run a MCMC exploration with Planck high- ℓ temperature likelihood and compare the results with the Planck published ones. We find good agreement between these two run of the Planck likelihood, meaning that our configuration is the same as that used for the Planck analysis.

We give results for our three likelihoods and compare them to the Planck likelihood run. We note that a Gaussian prior is imposed on the absolute map calibration for Planck likelihood $y_{cal} = 1 \pm 0.0025$, while we keep this value fixed to $y_{cal} = 1$. We adopt this choice after testing that including this parameter in the

explorations does not affect the results, apart from increasing the total number of parameters to be sampled.

We plot a comparison of the cosmological parameters estimated in Fig. 11, while the full list including derived parameters can be found in Table 3. The respective values for the Planck likelihood analysis can be found in Planck Collaboration XI et al. (2016), where Table 17 lists the cosmological parameters and Table 10 the nuisance parameters. Shifts of cosmological parameters in units of 1σ Planck error bars are presented in Table 4: for most parameters we observe a progressive shift increasing with the retained sky fraction, the most evident case being for n_s . On the whole, parameters show at most 1σ deviation with respect to the Planck analysis, with the only exception of ω_b for $f_{sky} = 0.3$, which shows a deviation of -2.04σ , and n_s for $f_{sky} = 0.6$, which shows a deviation of 1.48σ .

At low f_{sky} the residuals are weak and not clearly constrained by the nuisance model. As seen in simulations, there is an uncertainty in the value of the nuisance parameters that induces a shift in the cosmological parameters. In Fig. 12 we can see that nuisance parameters are consistent with zero and are also strongly degenerate among them. Some degeneracies are also visible with the cosmological parameters, as for example between $A_s e^{-2\tau}$ and A_{dust} . Due to the strong correlation between all cosmological parameters, these degeneracies can induce biases. Also, as noted by Huffenberger et al. (2006), the parameter n_s is particularly sensitive to incorrect subtraction of the point source component, since a residual of point sources can mimic a different tilt of the CMB angular power spectrum. The biases we obtain are representative of the uncertainty on the determination of the foreground model. For Like-F03 we perform an analysis without any nuisance parameters, finding smaller shifts with respect to the reference configuration. This is further evidence for the existence of degeneracies between cosmological and weakly constrained nuisance parameters. Results are shown in the ‘‘No nuisance’’ column of

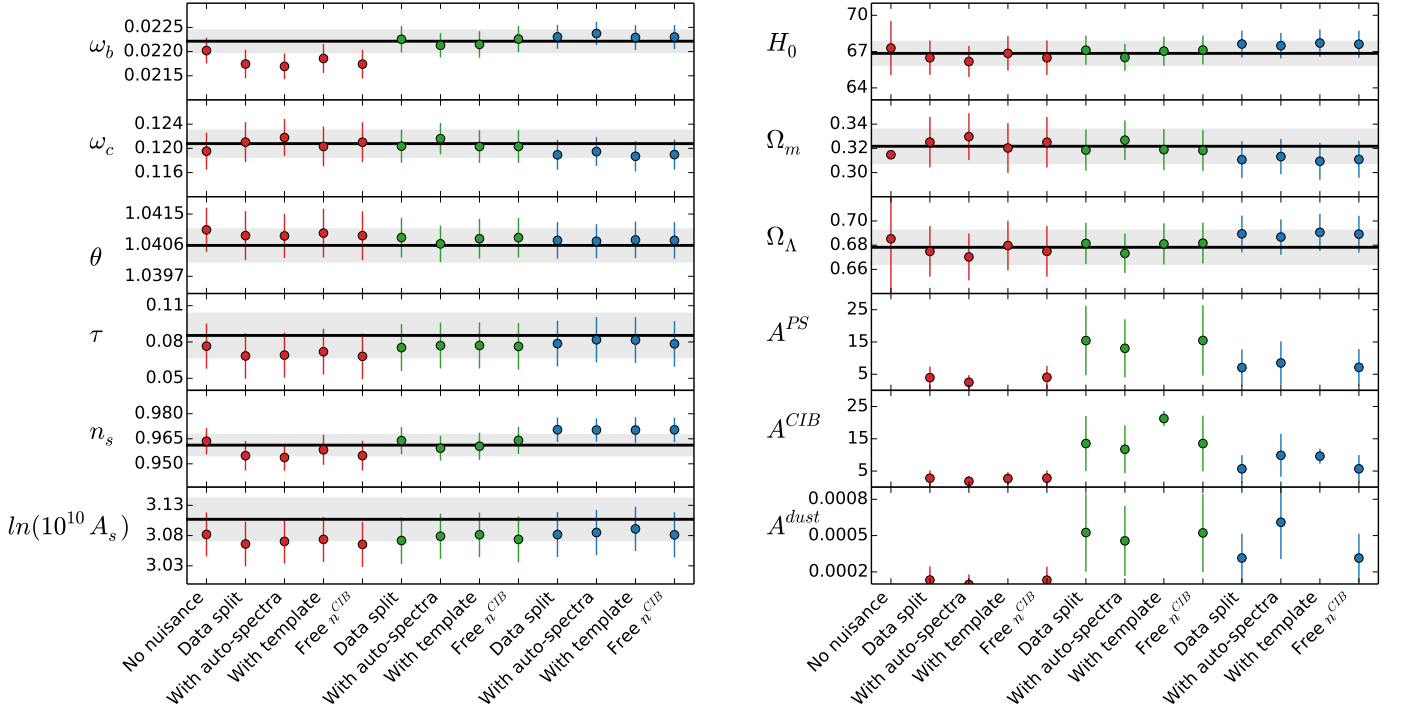


Fig. 11: Marginal mean and 68% CL error bars for cosmological parameters obtained with Like-F03 in red, Like-F05 in green and Like-F06 in blue. For comparison, Planck 2015 high- ℓ temperature likelihood results are shown in the background, with the marginal mean drawn in black and 68% CL as a grey band. On the left we show the six standard Λ CDM cosmological parameters and on the right some derived and nuisance parameters. Nuisance parameters show no Planck comparison since they are specific to the likelihood. The values of nuisance parameters are in units of μK^2 . The template amplitude is shown in the A^{CIB} column since its shape is very close to that of the CIB term in the nuisance physical model.

Table 3: Results of the MCMC exploration with the three considered likelihoods: Like-F03, Like-F05 and Like-F06. Constraints on parameters are given as marginal mean with 68% CL error on: main parameters (top), nuisance parameters (middle) and derived parameters (bottom). The Planck quoted values are obtained with Planck 2015 high- ℓ likelihood.

Parameter	Like-F03	Like-F05	Like-F06
$\omega_b h^2$	0.02174 ± 0.00030	0.02225 ± 0.00027	0.02230 ± 0.00025
$\omega_c h^2$	0.1210 ± 0.0033	0.1204 ± 0.0027	0.1189 ± 0.0025
$100\theta_{MC}$	1.04088 ± 0.00071	1.04082 ± 0.00057	1.04074 ± 0.00053
$\ln(10^{10} A_s)$	3.066 ± 0.037	3.072 ± 0.039	3.082 ± 0.037
n_s	0.9548 ± 0.0089	0.9639 ± 0.0081	0.9704 ± 0.0073
τ	0.068 ± 0.019	0.075 ± 0.019	0.079 ± 0.019
A^{PS}	3.9 ± 3.4	15 ± 11	7.0 ± 5.6
A^{CIB}	2.8 ± 2.4	1341 ± 8.6	5.7 ± 4.3
A^{dust}	0.00013 ± 0.00011	0.0052 ± 0.00032	0.00031 ± 0.00020
H_0	66.5 ± 1.4	67.1 ± 1.2	67.6 ± 1.1
Ω_m	0.325 ± 0.021	0.318 ± 0.017	0.311 ± 0.015
Ω_Λ	0.675 ± 0.021	0.681 ± 0.017	0.690 ± 0.015

Fig. 11. This analysis is only possible for $f_{sky}=0.3$ since the level of residuals is too high for the other two masks.

The results of the analysis using a template are also shown in Fig. 11. This configuration performs slightly better, especially at low f_{sky} , reducing the biases on n_s and ω_b . No significant improvement is seen however at high f_{sky} . The more, the total foreground power detected by the template is lower at $f_{sky} = 0.6$ than at $f_{sky} = 0.5$. This suggests that for high sky fraction the template is not anymore representative of the residual contamination in the CMB spectrum. This is partially true also for the physical nu-

sance model, meaning that the residuals at large sky fraction are not well represented by neither model.

We note that the biases observed in the data analysis are different from those observed in simulations. This suggests that the foreground complexity is not well accounted for in our simulations and that the correct choice of the nuisance model strongly depends on the details of the foreground contamination.

Table 4: Shift of parameters between the three data likelihoods Like-F03, Like-F05 and Like-F06 and the Planck high- ℓ likelihood results in units of 1σ Planck errors.

Parameter	Like-F03	Like-F05	Like-F06
$\omega_b h^2$	-2.04	0.17	0.39
$\omega_c h^2$	0.11	-0.19	-0.84
$100\theta_{MC}$	0.59	0.48	0.30
τ	-0.93	-0.55	-0.37
n_s	-1.02	0.43	1.48
$\log(10^{10}A_s)$	-1.17	-1.00	-0.72
H_0	-0.37	0.26	0.79
Ω_m	0.24	-0.23	-0.79
Ω_Λ	-0.24	0.23	0.79

6.4. Cross-tests on data

Results presented in Tables 4 and 3 refer to the main exploration detailed above. As a cross-check we present in Fig. 11 results of two different configurations. The first uses best fit CMB spectra as obtained from Sect. 5.4, that is using both auto- and cross-spectra to build covariance matrices. The second adds as nuisance parameter the CIB index which defines the angular power spectrum shape of the CIB residuals as ℓ^{nCIB} . This parameter is varied with a Gaussian prior $n^{CIB} = -1.3 \pm 0.2$. We observe no relevant shift in the obtained cosmological parameters from this two additional configurations.

We also obtain cosmological parameters from the best fit obtained using the 857 GHz channel as described in Sect. 5.3. We run MCMC for $f_{sky} = 0.6$ on SET3 simulations and obtain cosmological parameters which are consistent with those shown in Fig. 10 within maximum 0.022σ (σ here is the scatter of the marginal mean among various simulations). Instead, on the Planck data analysis, cosmological parameters are more strongly biased than those obtained without the 857 GHz channel, in particular n_s and ω_b . While the increase in foreground residuals in the spectrum is modest, we expect their characteristics to be quite complex and not adjustable by the minimal nuisance model we use.

7. Conclusions

We have studied a new configuration of the SMICA method to estimate the CMB angular power spectrum directly via component separation. This configuration uses only cross-angular power spectra between half-mission data split, thus avoiding the noise bias present in autospectra. We use a constrained foreground model that targets the extragalactic point sources emission. This is particularly important since the point sources level is degenerate with the CMB at small scales. Using SMICA, we jointly fit for the CMB power spectrum, the point sources emission law and other foregrounds angular spectra and frequency emission, such as dust and clustered CIB.

We obtain an estimate for the point sources emission law that is consistent with independent estimates in *Planck Collaboration* analysis. We recover a fit of the CMB angular power spectrum that we use to derive cosmological parameters through an MCMC likelihood exploration, both on Planck 2015 data and simulations. To model the foreground residuals in the CMB spectra, two configurations of nuisance parameters are studied, a physical model and an artificial template based on results of simulations. In both cases the cosmological parameters we obtain for simulations and Planck data agree with the predicted values

of the *Planck Collaboration* analysis ([Planck Collaboration XIII et al. 2016](#)) within 1σ on average. The level of biases that we observe on the simulations shows us the level of bias to expect on the real data.

The observed shifts strongly depend on the foreground residuals and on the nuisance model of the likelihood. If the foreground residuals are weak, the nuisance parameters are not well constrained by the data, and their misvaluation can induce biases on the cosmological parameters. When the foreground contamination is stronger the foreground model is better constrained and the biases are reduced. However the residuals characteristics need careful modeling, and a minimal model as that used in this work is not sufficient to describe them. We observe this both on simulations and on Planck data. Using a single foreground template for nuisance has the advantage of having less parameters to fit, however the shape of this template is not universal and again depends on the foregrounds characteristics.

In conclusion we observe that a blind method as SMICA with an adapted model for the extragalactic foregrounds can recover an estimate of the CMB power spectrum which has a very low foreground residual content. However, in order to use this estimate for cosmological purposes, a deep knowledge and careful modeling of the shape of the foreground residuals is needed. The same is true also for the Planck likelihood analysis in [Planck Collaboration XV et al. \(2014\)](#), thus it is not clear whether this blind approach grants any advantage, at least for the CMB temperature analysis, where foregrounds are particularly complex. When considering polarization, a blind approach could still be useful since the small scales foreground contamination is more simple, while SMICA has demonstrated its ability to deal with large scale complex contamination ([Planck Collaboration XII 2014](#)). Also, using a zone approach with SMICA that would take into account the variability of galactic foregrounds on the sky could improve the efficiency of component separation and thus improve the cosmological parameters estimation.

Acknowledgements. UC wishes to thank Aurélien Benoit-Lévy for suggestions on masks treatment, Silvia Galli for discussions on simulations and cosmological parameters, Éric Hivon for tips on the use of HEALPix, Marius Millea for helpful insight on radio point sources and CosmoSlik and Mario Ballardini for helpful suggestions on CosmoMC. This work has made use of the Horizon Cluster hosted by Institut d’Astrophysique de Paris. We thank Stephane Rouberol for running smoothly this cluster for us. UC has been supported within the Labex ILP (reference ANR-10-LABX-63) part of the Idex SUPER, and received financial state aid managed by the Agence Nationale de la Recherche, as part of the programme Investissements d’avenir under the reference ANR-11-IDEX-0004-02. This research used publicly available Planck data.

References

- Basak, S. & Delabrouille, J. 2012, MNRAS, 419, 1163
- Basak, S. & Delabrouille, J. 2013, MNRAS, 435, 18
- Bedini, L., Herranz, D., Salerno, E., et al. 2005, EURASIP Journal on Applied Signal Processing, 2005, 2400
- Bobin, J., Moudden, Y., Starck, J.-L., Fadili, J., & Aghanim, N. 2008, Statistical Methodology, 5, 307
- Bobin, J., Starck, J.-L., Sureau, F., & Basak, S. 2013, A&A, 550, A73
- Bonaldi, A., Bedini, L., Salerno, E., Baccigalupi, C., & De Zotti, G. 2006, Monthly Notices of the Royal Astronomical Society, 373, 271
- Cardoso, J.-F. 2017, in Latent Variable Analysis and Signal Separation, ed. P. Tichavský, M. Babaie-Zadeh, O. J. Michel, & N. Thirion-Moreau (Cham: Springer International Publishing), 403–413
- Cardoso, J.-F., Le Jeune, M., Delabrouille, J., Betoule, M., & Patanchon, G. 2008, IEEE Journal of Selected Topics in Signal Processing, 2, 735
- Chon, G., Challinor, A., Prunet, S., Hivon, E., & Szapudi, I. 2004, MNRAS, 350, 914
- Delabrouille, J., Cardoso, J.-F., Le Jeune, M., et al. 2009, A&A, 493, 835
- Delabrouille, J., Cardoso, J.-F., & Patanchon, G. 2003, MNRAS, 346, 1089

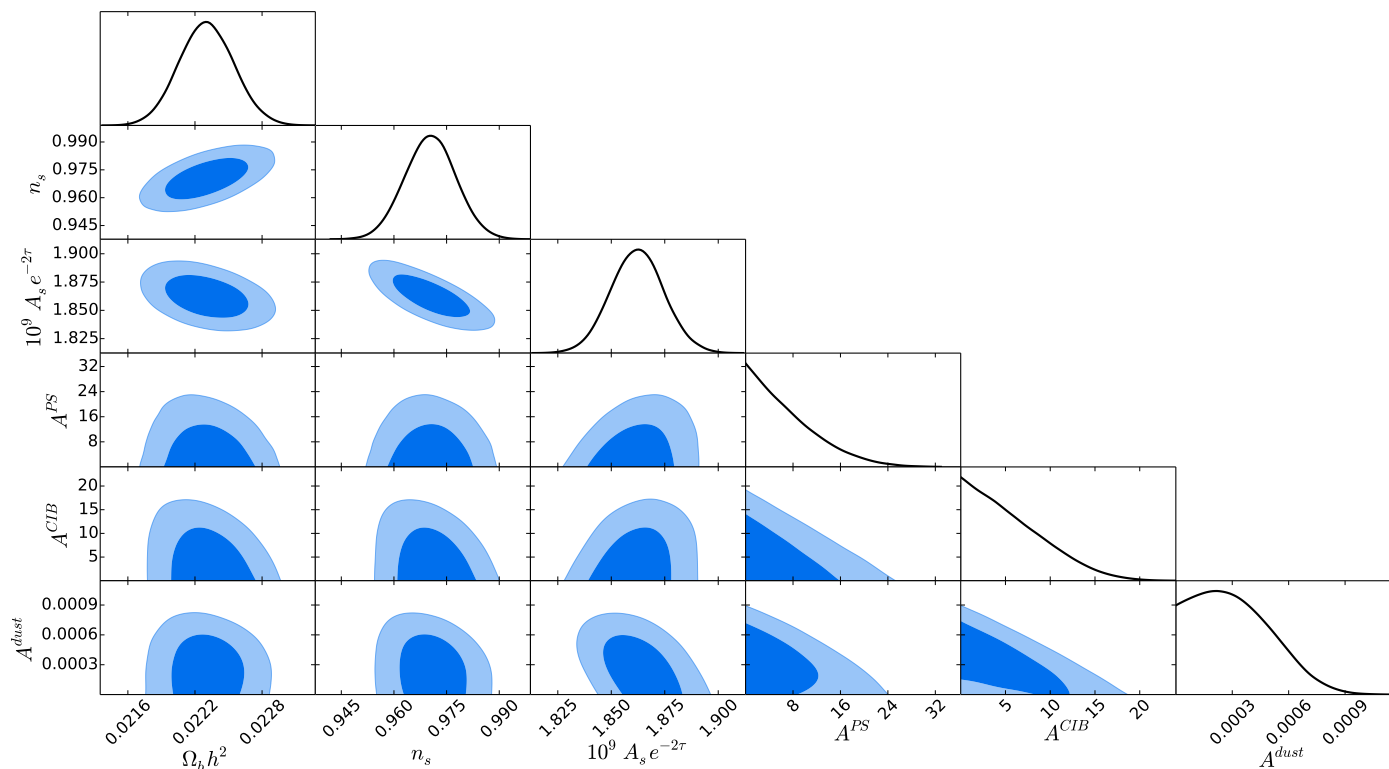


Fig. 12: Triangle plot showing the relation between the main cosmological parameters and the nuisance parameters, for the analysis on data with $f_{\text{sky}} = 0.6$. Similar plots are obtained for SET3 simulations and for different f_{sky} . The blue and light-blue contours represent the 68% and 95% CL respectively.

- Eriksen, H. K., Jewell, J. B., Dickinson, C., et al. 2008, *The Astrophysical Journal*, 676, 10
- Eriksen, H. K., O'Dwyer, I. J., Jewell, J. B., et al. 2004, *Astrophysical Journal Supplement*, 155, 227
- Fendt, W. A. & Wandelt, B. D. 2007, Submitted to: *Astrophys. J.* [arXiv:0712.0194]
- Fernández-Cobos, R., Vielva, P., Barreiro, R. B., & Martínez-González, E. 2012, *MNRAS*, 420, 2162
- Górski, K. M., Hivon, E., Banday, A. J., et al. 2005, *ApJ*, 622, 759
- Hall, N. R., Keisler, R., Knox, L., et al. 2010, *ApJ*, 718, 632
- Hinshaw, G., Spergel, D. N., Verde, L., et al. 2003, *ApJS*, 148, 135
- Huffenberger, K. M., Eriksen, H. K., & Hansen, F. K. 2006, *ApJ*, 651, L81
- Ichiki, K. 2014, *Progress of Theoretical and Experimental Physics*, 2014, 06B109
- Lacasa, F., Aghanim, N., Kunz, M., & Frommert, M. 2012, *MNRAS*, 421, 1982
- Lewis, A. & Bridle, S. 2002, *Phys. Rev. D*, 66, 103511
- Lewis, A. & Bridle, S. 2002, *Phys. Rev.*, D66, 103511
- Maino, D., Farusi, A., Baccigalupi, C., et al. 2002, *MNRAS*, 334, 53
- Mak, D. S. Y., Challinor, A., Efstathiou, G., & Lagache, G. 2017, *Monthly Notices of the Royal Astronomical Society*, 466, 286
- Millea, M. 2017, *CosmoSlik: Cosmology sampler of likelihoods*, *Astrophysics Source Code Library*
- Millea, M., Doré, O., Dudley, J., et al. 2012, *The Astrophysical Journal*, 746, 4
- Paoletti, D., Aghanim, N., Douspis, M., et al. 2012, *MNRAS*, 426, 496
- Patanchon, G., Cardoso, J.-F., Delabrouille, J., & Vielva, P. 2005, *MNRAS*, 364, 1185
- Planck Collaboration, Ade, P. A. R., Aghanim, N., et al. 2016a, *A&A*, 594, A25
- Planck Collaboration, Ade, P. A. R., Aghanim, N., et al. 2016b, *A&A*, 594, A17
- Planck Collaboration, Ade, P. A. R., Aghanim, N., et al. 2016c, *A&A*, 594, A15
- Planck Collaboration IX, Adam, R., Ade, P. A. R., et al. 2016, *A&A*, 594, A9
- Planck Collaboration X, Adam, R., Ade, P. A. R., et al. 2016, *A&A*, 594, A10
- Planck Collaboration XI, Aghanim, N., Arnaud, M., et al. 2016, *A&A*, 594, A11
- Planck Collaboration XII. 2014, *A&A*, 571, A12
- Planck Collaboration XIII, Ade, P. A. R., Aghanim, N., et al. 2016, *A&A*, 594, A13
- Planck Collaboration XLVIII, Aghanim, N., Ashdown, M., et al. 2016, *A&A*, 596, A109
- Planck Collaboration XV, Ade, P. A. R., Aghanim, N., et al. 2014, *A&A*, 571, A15
- Planck Collaboration XXX, Ade, P. A. R., Aghanim, N., et al. 2014, *A&A*, 571, A30
- Remazeilles, M., Delabrouille, J., & Cardoso, J.-F. 2011, *MNRAS*, 418, 467
- Rogers, K. K., Peiris, H. V., Leistedt, B., McEwen, J. D., & Pontzen, A. 2016, *MNRAS*, 460, 3014
- Sudevan, V., Aluri, P. K., Yadav, S. K., Saha, R., & Souradeep, T. 2017, *The Astrophysical Journal*, 842, 62
- Tegmark, M. & Efstathiou, G. 1996, *MNRAS*, 281, 1297
- Vansyngel, F., Wandelt, B. D., Cardoso, J.-F., & Benabed, K. 2016, *A&A*, 588, A113
- Zhang, P., Zhang, J., & Zhang, L. 2016, *ArXiv e-prints* [arXiv:1608.03707]

Appendix A: Masks

The masks we use are the sum of a galactic and a point source part: while the point source part is the same for all masks, the galactic sky coverage changes. For the galactic part we create a set of masks starting from those delivered by the *Planck Collaboration*⁶. From these, we choose the three galactic masks of retained sky fraction $f_{sky} = 0.4, 0.6, 0.7$. These mask are not apodised, thus need to be smoothed at the edges. First we smooth them with a Gaussian beam of $FWHM = 3^\circ$ and then we threshold them to obtain a new set of slightly smaller masks of $f_{sky} = 0.45, 0.65, 0.75$. This step is needed in order to avoid that the subsequent apodisation results in a large decrease of the retained sky fraction. Using the *process_mask* function of the HEALPix package, for each of these masks we obtain a distance map, i.e., a map in which each pixel contains the distance to the nearest masked pixel. Such a map is used to apodise the galactic masks by convolution with a Gaussian of $FWHM = 4^\circ$. The use of distance maps instead of a simple Gaussian smoothing avoids leakage into the original mask.

We create the point source mask based on the Planck 2015 Catalogue of Compact Sources⁷ as the union of the point sources masks at the five frequency channels of interest. This point source mask is apodised with $FWHM = 1^\circ$, using a distance map. We combine our point source apodised mask with our apodised galactic masks to obtain the final set of masks we use in this analysis. Their respective retained sky fraction is $f_{sky}=0.31, 0.48, 0.57$, but to enhance readability we refer to them as $f_{sky}=0.3, 0.5, 0.6$ throughout the text.

We also create a second set of masks for cross-check analysis that include point sources at 857 GHz. These masks have a similar sky fraction to the leading set, and they are used only for the tests performed in Sect. 5.3

⁶ available for download at <http://pla.esac.esa.int> (*HFI_Mask_GalPlane-apo0_2048_R2.00.fits*)

⁷ v2.0, also available for download at <http://pla.esac.esa.int>